Recognition of Power Quality Disturbances Using AFD Based Features and Graph Convolutional Network

Yanjiang Qiu[a], Chitin Hon[b], Tao Qian[c,*]

[a]*School of Computer Science and Engineering, Faculty of Innovation Engineering, Macau University of Science and Technology, Macau, 999078, China*
[b]*Respiratory Disease AI Laboratory in Epidemic Intelligence and Applications of Medical Big Data Instruments, Institute of Systems Engineering, Macau University of Science and Technology, Macau, 999078, China*
[c]*Macau Center for Mathematical Sciences, Macau University of Science and Technology, Macau, 999078, China*

Abstract

With the continuous development of modern power systems, more and more nonlinear devices are being used, which leads to increasingly serious power quality disturbance (PQD) problems. To ensure the stable operation of power systems, the accurate recognition of PQDs is both critical and challenging. This paper proposes a novel method for PQD recognition based on adaptive Fourier transform (AFD) and graph convolutional network (GCN), referred to as the AFD-GCN scheme. The architecture of the AFD-GCN scheme consists of three main stages: signal analysis, feature extraction, and PQD recognition. First, a new method suitable for analyzing time-varying non-stationary signals, namely AFD, is introduced. AFD not only adaptively represents the original signal sparsely but also transforms the signal into the time-frequency domain with high resolution, providing an accurate understanding of the signal. Second, ten feature calculation methods based on AFD are proposed. Third, considering the potential relationships between different PQDs, a graph describing their connections is constructed. Finally, the AFD-based features and the proposed graph structure are input into the GCN to achieve the recognition of different PQDs. The feasibility effectiveness, and robustness of the AFD-GCN scheme for PQD recognition are validated through experiments using both synthetic and real-world signals.

*Corresponding author.
Email address: tqian@must.edu.mo (Tao Qian)

Preprint not peer reviewed

This preprint research paper has not been peer reviewed. Electronic copy available at: https://ssrn.com/abstract=5229636

Keywords: Power quality disturbance, adaptive Fourier decomposition, graph convolutional network, marginal distribution, feature extraction.

1. Introduction

The output of wind and solar energy is inherently intermittent and variable, leading to voltage and frequency deviations in the modern power systems [1]. The regulation capacity of conventional power sources may be inadequate to compensate for these fluctuations, which may lead to power quality disturbances (PQDs) [1, 2]. Renewable energy generation systems typically integrate a significant number of power electronic converters, which exhibit nonlinear behavior and generate harmonics and voltage fluctuations during operation [3]. Additionally, renewable energy units controlled by virtual synchronous machines may experience subsynchronous oscillations due to parameter mismatches, which endanger equipment safety [4, 5]. Therefore, accurate recognition and monitoring of PQDs are essential for ensuring the stable operation of modern power systems.

PQDs commonly include various issues such as the signal attenuation, sag, swell, interruption, flicker, subsynchronous oscillation, oscillatory transient, impulsive transient, harmonic, multiple notches and spikes, among others [6, 7]. The process of PQD recognition can be summarized into three key steps, namely signal analysis, feature extraction and classification. One of the advantages of the three-step PQD recognition method is that it can be easily embedded into hardware. Therefore, it has been widely recognized and applied in engineering [8]. In the signal analysis and feature extraction stage, the time-domain feature is computationally efficient for simple classification tasks [8]. However, it fails to capture frequency-domain features, depends on stationary data, and is noise-sensitive, limiting its applicability to complex scenarios. Fast Fourier transform (FFT) can effectively extract periodic components from stationary signals but is unable to capture transient features in non-stationary ones [9]. Additionally, both the fence effect and spectral leakage may compromise the reliability of the extracted features [10]. Short-time Fourier transform (STFT) can mine signal information from two different perspectives: time and frequency [11, 12]. However, the resolution of STFT is fixed, which makes STFT unable to adapt to the changes of different frequency components [10, 13]. Wavelet transform (WT) decomposes the signal using wavelet basis functions of different scales and positions, and

Preprint not peer reviewed

This preprint research paper has not been peer reviewed. Electronic copy available at: https://ssrn.com/abstract=5229636

can simultaneously extract the temporal locality and frequency features of the signal [14, 15, 16, 17]. Improper selection of wavelet bases in the WT algorithm may lead to inaccurate analysis results and even erroneous conclusions. Stockwell transform (ST) It can automatically adjust the width of the window function based on the frequency at different moments, thereby achieving higher time-frequency resolution for analyzing time-varying signals [9, 18, 19, 20]. However, the computational complexity of ST is high, and its signal analysis results are usually redundant, which poses significant challenges for its practical applications. Since Empirical mode decomposition (EMD) does not require predefined basis functions or assume specific characteristics of the signal, it can extract signal components with various scales directly from the data [21]. However, mode mixing may occur during the decomposition process, where different frequency components may be mixed within the same intrinsic mode function (IMF), or components with the same frequency may appear in multiple IMFs. Toward this, several improved methods have been proposed, including variational mode decomposition (VMD) [22], complete ensemble empirical mode decomposition with adaptive noise (CEEMDAN) [8]. The combination of EMD and Hilbert transform forms the Hilbert-Huang transform (HHT) [21, 23]. It can characterize signal features from various spectral perspectives [23], but the inherent defects of EMD can affect the results of feature extraction.

The commonly used classifiers in traditional machine learning include naive Bayes (NB) [24], decision trees (DT) [22], support vector machines (SVM) [17], and K-nearest neighbor (KNN) [25]. For small datasets, these models can typically achieve more accurate results rapidly. However, they are not well-suited for fitting nonlinear models and lack sufficient capability to handle high-dimensional data. Consequently, some artificial intelligence based methods have been introduced, such as probabilistic neural networks (PNN) [16], artificial neural networks (ANN) [9], back propagation neural networks (BPNN) [26]. They offer significant advantages when dealing with the complex and high-dimensional data. Nevertheless, the decision-making processes of these models are complex. Moreover, their training process usually requires a large amount of annotated data, which may lead to overfitting and incorrect recognition of PQDs when the data is insufficient. In addition, some classifiers based on neural networks have also been applied to PQD recognition [6, 27]. In summary, although these models demonstrate some effectiveness in learning differences within the data, they often fail to capture the underlying connections. Consequently, in modern power systems,

Preprint not peer reviewed

This preprint research paper has not been peer reviewed. Electronic copy available at: https://ssrn.com/abstract=5229636

complex PQD identification tasks may pose significant challenges for them.

In recent years, Qian et al. [28, 29] proposed a method for non-stationary signal analysis, known as adaptive Fourier decomposition (AFD). This method adaptively searches for a rational orthogonal function system in the Hardy space through an iterative process, aiming to achieve the sparse representation of signals. Furthermore, the transient time-frequency distribution (TTFD) and marginal distribution (MD) based on AFD have been introduced for signal analysis in the time-frequency domain [30]. Given the advantages of AFD in non-stationary signal analysis, this article proposes using AFD to analyze PQD signals. Based on the analysis results, 10 feature extraction methods are developed. In addition, considering the intrinsic relationship between different PQDs, this article proposes a graph structure to represent these relationships and further introduces graph convolutional network (GCN) as a classifier for PQD recognition. The main contributions of this article are as follows:

(1) This article proposes the use of AFD for the sparse representation of PQD signals. Furthermore, based on AFD, TTFD is employed to analyze the time-frequency characteristics of PQD signals, while MD is utilized to examine their average energy distribution across time and frequency. This approach provides a novel perspective for the analysis of PQD signals.

(2) Based on the AFD-based signal analysis, 10 feature extraction methods are developed. The extracted features, referred to as AFD-based features, characterize the distinctions between different PQDs from the perspectives of time domain, frequency domain, AFD domain, time-frequency domain, and statistics. They facilitate more effective recognition for PQDs by classifiers.

(3) Considering the relationships between different PQDs, this article constructs a graph structure to represent their connections. By integrating GCN with AFD-based features, an AFD-GCN scheme is proposed for recognizing different PQDs. In this scheme, GCN learns both the connections and distinctions between PQDs based on the proposed graph structure and AFD-based features, which enables the classifier to comprehensively and accurately capture the relationships between complicated PQDs and ensure the accuracy of PQD recognition.

The writing of this article is organized as follows. Section 2 introduces the AFD-based signal analysis, AFD-based feature extraction methods, and the proposed AFD-GCN scheme for PQD recognition. Section 3 provides the simulations and hardware experiment to validate the effectiveness of the proposed scheme. The conclusions of this article are drawn in Section 4.

Preprint not peer reviewed

This preprint research paper has not been peer reviewed. Electronic copy available at: https://ssrn.com/abstract=5229636

2. Methodology

This article mainly focus on 12 PQD signals listed in Table 1, which are modified from Table 1 in [6] and [16]. In Table 1, when $t > 0$, $u(t) = 1$; Otherwise, $u(t) = 0$. And, $T = 1/F_0$. All parameter ranges meet the requirements of the IEEE-1159 standard [31]. This section provides a detailed introduction to the AFD-based signal analysis, AFD-based feature extraction methods and the proposed AFD-GCN scheme. The theory of AFD is described in [28], and the software system design is detailed in [29].

2.1. AFD-based signal analysis

An electrical signal containing arbitrary PQD can be written as

$$g(t) = A(1 + h(t)) \cos 2\pi F_0 t, \tag{1}$$

where A and F_0 denote the amplitude and frequency of the fundamental component, respectively. $h(t)$ represents the PQD function. $f(t) = A(1 + h(t))$ can be regarded as the phasor of fundamental component. To extract the features of PQD, $f(t)$ is analyzed. According to the Fourier decomposition, $f(t)$ can be decomposed into

$$f(t) = \sum_{m=-\infty}^{+\infty} c_m e^{\mathbf{i}mt}, \sum_{m=-\infty}^{+\infty} |c_m|^2 < +\infty, \tag{2}$$

where the Fourier coefficient $c_m = \left\langle f, e^{\mathbf{i}mt} \right\rangle = \frac{1}{2\pi} \int_0^{2\pi} f(t) e^{-\mathbf{i}mt} dt$. Let $\mathbb{D}$ be an open unit disc centered on the origin in the complex plane. $\mathbb{T}$ represents the boundary of $\mathbb{D}$. $H^2(\mathbb{D})$ is the complex Hardy space on $\mathbb{D}$. The complex Hardy space $H^2(\mathbb{T})$ is a closed subspace of $H^2(\mathbb{D})$. Due to the conjugate symmetry of Fourier spectra, the function $f(t)$ can be decomposed into

$$f(t) = \sum_{m=0}^{\infty} \left(c_m e^{\mathbf{i}mt} + c_m e^{-\mathbf{i}mt} \right) - c_0 \triangleq \sum_{m=0}^{\infty} \left(f_m^+ \left(e^{\mathbf{i}t} \right) + f_m^- \left(e^{\mathbf{i}t} \right) \right) - c_0 \tag{3}$$

$$= 2\mathbf{Re} \left\{ \sum_{m=0}^{\infty} f_m^+ \left(e^{\mathbf{i}t} \right) \right\} - c_0 = 2\mathbf{Re} \left\{ f^+ \left(e^{\mathbf{i}t} \right) \right\} - c_0. \tag{4}$$

Here, f^+ and f^- denote the positive and negative frequency parts of f, respectively. $\mathbf{Re}\{\cdot\}$ is the real part operator. The analytic function $f^+ \left(e^{\mathbf{i}t} \right)$

Preprint not peer reviewed

This preprint research paper has not been peer reviewed. Electronic copy available at: https://ssrn.com/abstract=5229636

Table 1: Model of PQD signals.

PQD	Label	Mathematical model
Normal signal	C1	$g(t) = A\cos(wt)$, $A = 1$ pu, $w = 100\pi t$.
Attenuation	C2	$g(t) = Ae^{-10\log(A/\mu)t}\cos(wt)$, $0.1A \leq \mu \leq 0.9A$.
Sag	C3	$g(t) = A[1-\alpha(u(t-t_1)-u(t-t_2))]\cos(wt)$, $0.1 \leq \alpha \leq 0.9$, $T \leq t_2 - t_1 \leq 9T$.
Swell	C4	$g(t) = A[1+\alpha(u(t-t_1)-u(t-t_2))]\cos(wt)$, $0.1 \leq \alpha \leq 0.8$, $T \leq t_2 - t_1 \leq 9T$.
Interruption	C5	$g(t) = A[1-\alpha(u(t-t_1)-u(t-t_2))]\cos(wt)$, $0.9 \leq \alpha \leq 1$, $T \leq t_2 - t_1 \leq 9T$.
Flicker	C6	$g(t) = A[1+\alpha\cos(\beta wt)]\cos(wt)$, $0.1 \leq \alpha \leq 0.2$, $0.1 \leq \beta \leq 0.4$.
Subsynchronous oscillation	C7	$g(t) = A\left[\cos(wt) + \alpha e^{-10\log(A/\mu)t}\cos(\beta wt)\right]$, $0.1A \leq \mu \leq 0.9A$; $0.1 \leq \alpha \leq 0.8$, $0.2 \leq \beta \leq 0.8$.
Oscillatory transient	C8	$g(t) = A\cos(wt) + A\alpha e^{(t-t_1)/\tau}\cos(w_m(t-t_1))(u(t_2)-u(t_1))$, $0.1 \leq \alpha \leq 0.8$, $0.05T \leq t_2 - t_1 \leq 3T$, $300 \leq w_m \leq 900$ Hz, $8 \leq \tau \leq 40$ ms.
Impulsive transient	C9	$g(t) = A\left[\cos(wt) + \alpha e^{(t-t_1)/\tau}(u(t_2)-u(t_1))\right]$, $0.1 \leq \alpha \leq 0.8$; $8 \leq \tau \leq 40$ ms, $0.5T \leq t_2 - t_1 \leq 3T$.
Harmonic	C10	$g(t) = A\cos(wt) + A\alpha_1\cos(3wt) + A\alpha_2\cos(5wt) + A\alpha_3\cos(7wt)$, $0.05 \leq \alpha_1, \alpha_2, \alpha_3 \leq 0.15$.
Multiple notches	C11	$g(t) = A\cos(wt) - \text{sign}(\cos(wt)) \times \sum_{m=1}^{10}\alpha\left[u\left(t-\left(t_1-\frac{m}{T}\right)\right) - u\left(t-\left(t_2-\frac{m}{T}\right)\right)\right]$, $0.1 \leq \alpha \leq 0.4$, $0 \leq t_1, t_2 \leq 0.5T$, $0.01T \leq t_2 - t_1 \leq 0.05T$.
Multiple spikes	C12	$g(t) = A\cos(wt) + \text{sign}(\cos(wt)) \times \sum_{m=1}^{10}\alpha\left[u\left(t-\left(t_1-\frac{m}{T}\right)\right) - u\left(t-\left(t_2-\frac{m}{T}\right)\right)\right]$, $0.1 \leq \alpha \leq 0.4$, $0 \leq t_1, t_2 \leq 0.5T$, $0.01T \leq t_2 - t_1 \leq 0.05T$.

can be calculated by $f^+\left(e^{\mathbf{i}t}\right) = \frac{1}{2}\left(f(t) + \mathbf{i}\mathcal{H}f(t) + c_0\right)$, where $\mathcal{H}f$ is the Hilbert transformation of f. Thus, $f(t) = 2\mathbf{Re}\left\{f^+\left(e^{\mathbf{i}t}\right)\right\}$.

Core AFD is based on the rational orthogonal function system in $H^2(\mathbb{D})$, called the Takenaka-Malmquist (TM) system and denoted as $\left\{B_n\left(e^{\mathbf{i}t}\right)\right\}_{n=1}^{\infty}$,

Preprint not peer reviewed

This preprint research paper has not been peer reviewed. Electronic copy available at: https://ssrn.com/abstract=5229636

$$B_n\left(e^{\mathbf{i}t}\right)=\frac{\sqrt{1-|a_n|^2}}{1-\bar{a}_n e^{\mathbf{i}t}}\prod_{l=1}^{n-1}\frac{e^{\mathbf{i}t}-a_l}{1-\bar{a}_l e^{\mathbf{i}t}},a_l\in\mathbb{D}, \tag{5}$$

where $\bar{a}_l$ represents the complex conjugate of a_l. For $a_n\in\mathbb{D}$, $e_{a_n}\left(e^{\mathbf{i}t}\right)=\frac{\sqrt{1-|a_n|^2}}{1-\bar{a}_n e^{\mathbf{i}t}}$. The set $\{e_a\}_{a\in\mathbb{D}}$ forms a dictionary in $H^2(\mathbb{D})$, which is also the reproducing kernels of $H^2(\mathbb{D})$. The main idea of Core AFD is to adaptively expand $f\left(e^{\mathbf{i}t}\right)\in H^2(\mathbb{T})$ through the TM system. After being decomposed into N level by AFD, $f\left(e^{\mathbf{i}t}\right)$ can be written as

$$f\left(e^{\mathbf{i}t}\right)=\sum_{n=1}^{N}\left\langle f_n,e_{a_n}\right\rangle B_n\left(e^{\mathbf{i}t}\right)+\gamma_N\left(e^{\mathbf{i}t}\right), \tag{6}$$

$$\gamma_N\left(e^{\mathbf{i}t}\right)=f_{N+1}\left(e^{\mathbf{i}t}\right)\prod_{l=1}^{N}\frac{e^{\mathbf{i}t}-a_l}{1-\bar{a}_l e^{\mathbf{i}t}}, \tag{7}$$

$$f_{N+1}\left(e^{\mathbf{i}t}\right)=\frac{f_N\left(e^{\mathbf{i}t}\right)-\left\langle f_N,e_{a_N}\right\rangle e_{a_N}\left(e^{\mathbf{i}t}\right)}{\frac{e^{\mathbf{i}t}-a_N}{1-\bar{a}_N e^{\mathbf{i}t}}}. \tag{8}$$

The parameter a_n in (6) is selected by

$$a_n=\arg\max\left\{\left|\left\langle f_n,e_a\right\rangle\right|^2:a\in\mathbb{D}\right\}, \tag{9}$$

which is called the maximal selection principle (MSP). There exists a fact that $\left\langle f_n,e_{a_n}\right\rangle=\left\langle f,B_n\right\rangle$.

Each term of the AFD expression is a mono-component (MC) function [28]. Assume that the n-th MC function is $s_n(t)=\rho_n(t)\,e^{\mathbf{i}\theta_n(t)}$, where the instantaneous amplitude $\rho_n(t)=\left|\left\langle f,B_n\right\rangle B_n\left(e^{\mathbf{i}t}\right)\right|$, the instantaneous phase $\theta_n(t)=\mathcal{P}\left\{\left\langle f,B_n\right\rangle B_n\left(e^{\mathbf{i}t}\right)\right\}$ with phase operator $\mathcal{P}\{\cdot\}$. The derivative of $\theta_n(t)$ is considered to be the transient frequency of $s_n(t)$, that is,

$$\theta_n'(t)=\frac{|a_n|\cos\left(t-\mathcal{P}\{a_n\}\right)-|a_n|^2}{1-2|a_n|\cos\left(t-\mathcal{P}\{a_n\}\right)+|a_n|^2}+\sum_{l=1}^{n-1}\frac{1-|a_l|^2}{1-2|a_l|\cos\left(t-\mathcal{P}\{a_l\}\right)+|a_l|^2}. \tag{10}$$

After being decomposed into N terms by AFD, $f\left(e^{\mathbf{i}t}\right)$ can be seen as a superposition of MCs, which can be rewritten as $s(t):=\sum_{n=1}^{N}s_n(t)$. Thus, the TTFD of $s(t)$ is defined as

Preprint not peer reviewed

This preprint research paper has not been peer reviewed. Electronic copy available at: https://ssrn.com/abstract=5229636

$$P(t,\xi) \triangleq \sum_{n=1}^{N} \rho_n(t)\,\delta\left(\xi - \theta_n'(t)\right), \rho_n(t) = \frac{|\langle f, B_n\rangle|\sqrt{1-|a_n|^2}}{1-|a_n|\cos\left(t-\mathcal{P}\{a_n\}\right)+|a_n|^2}, \tag{11}$$

where $\delta(\cdot)$ represents the Dirac function, and Fourier frequency $\xi \in [0,\infty)$. The MD of $P(t,\xi)$ at the aspects of t and ξ are separately defined as

$$P_t(\xi) = \int_0^{2\pi} P(t,\xi)\,dt, P_\xi(t) = \int_0^{\infty} P(t,\xi)\,d\xi. \tag{12}$$

2.2. AFD-based feature extraction

By applying AFD to $f\left(e^{\mathbf{i}t}\right)$, we can obtain a sparse representation of $f(t)$. Furthermore, the corresponding TTFD and MDs can be calculated using (11) and (12), respectively. Based on this, 12 PQD signals listed in Table 1 were generated using MATLAB 2021a, with a sampling frequency of 2000 Hz and a sampling length of 10 cycles. The Core AFD was employed to decompose their phasors individually, and subsequently, their TTFD and MDs were calculated. The corresponding results are shown in Fig. 1.

As can be seen from Fig. 1, different PQD signals exhibit distinct waveform characteristics. Core AFD can accurately reconstruct all these waveforms. Moreover, from the perspectives of TTFD and MDs, there are significant differences between different phasors. Therefore, PQD features can be extracted by combining $f(t)$, $P_\xi(t)$, and $P_t(\xi)$. The discrete forms of $f(t)$, $P_\xi(t)$, and $P_t(\xi)$ are denoted as $\boldsymbol{f} = \{f(i)\}_{i=0}^{\zeta-1}$, $\boldsymbol{P_\xi} = \{P_\xi(i)\}_{i=0}^{\zeta-1}$, and $\boldsymbol{P_t} = \{P_t(i)\}_{i=0}^{\zeta-1}$, respectively, where ζ represents the number of sampling points. Then, 10 AFD-based features are proposed as

(1) Pulse factor of $\boldsymbol{f}$:

$$F1 := \frac{\max\{|\boldsymbol{f}|\}}{\sqrt{\frac{1}{\zeta}\sum_{i=0}^{\zeta-1} f^2(i)}}. \tag{13}$$

(2) Correlation coefficient between $\boldsymbol{f}$ and $\boldsymbol{P_\xi}$:

$$F2 := \frac{\sum_{i=0}^{\zeta-1}\left(f(i)-\tilde{\boldsymbol{f}}\right)\left(P_\xi(i)-\tilde{\boldsymbol{P}}_{\boldsymbol{\xi}}\right)}{\sqrt{\sum_{i=0}^{\zeta-1}\left(f(i)-\tilde{\boldsymbol{f}}\right)^2}\sqrt{\sum_{i=0}^{\zeta-1}\left(P_\xi(i)-\tilde{\boldsymbol{P}}_{\boldsymbol{\xi}}\right)^2}}, \tag{14}$$

Preprint not peer reviewed

This preprint research paper has not been peer reviewed. Electronic copy available at: https://ssrn.com/abstract=5229636

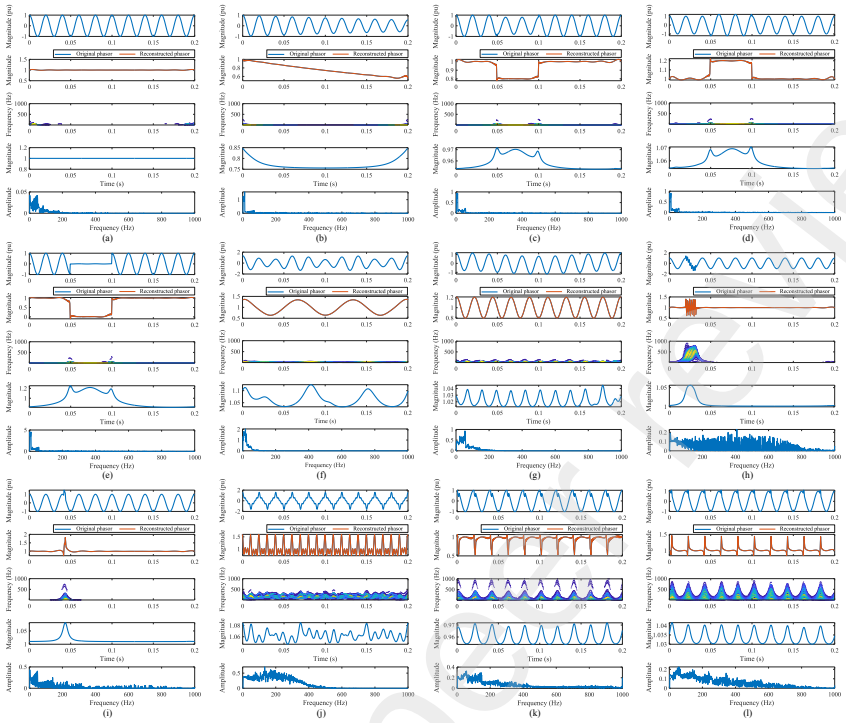


Figure 1: PQD signals and AFD-based analysis results. In each subgraph, the figures from top to bottom represent the original PQD signal, original phasor (blue line) and phasor reconstructed by AFD (orange line), TTFD, $P_{\xi}(t)$, and $P_t(\xi)$, respectively. (a) - (l) correspond to C1 - C12, respectively.

where $\tilde{\boldsymbol{f}} = \frac{1}{\zeta}\sum_{i=0}^{\zeta-1} f(i)$, $\tilde{\boldsymbol{P}}_{\boldsymbol{\xi}} = \frac{1}{\zeta}\sum_{i=0}^{\zeta-1} P_{\xi}(i)$.

(3) Difference between the maximum and minimum values of $|\boldsymbol{f}|$:

$$F3 := \begin{cases} \max\{|\boldsymbol{f}|\} - \min\{|\boldsymbol{f}|\}, & F2 \geq \epsilon \\ 0, & \text{otherwise} \end{cases}, \tag{15}$$

where ϵ represents the critical value of significant correlation.

(4) Time variation between the maximum and minimum values of the difference in $\boldsymbol{P}_{\boldsymbol{\xi}}$:

$$F4 := \begin{cases} |I_1 - I_2|, & F2 \geq \epsilon \\ 0, & \text{otherwise} \end{cases}, \tag{16}$$

where $I_1 = \arg\max\{P_{\xi}(i+1) - P_{\xi}(i) : 0 \leq i \leq \zeta - 2\}$,
$I_2 = \arg\min\{P_{\xi}(i+1) - P_{\xi}(i) : 0 \leq i \leq \zeta - 2\}$.

Preprint not peer reviewed

This preprint research paper has not been peer reviewed. Electronic copy available at: https://ssrn.com/abstract=5229636

(5) Difference between the maximum and minimum values of $\boldsymbol{P_\xi}$:

$$F5 := \max\{\boldsymbol{P_\xi}\} - \min\{\boldsymbol{P_\xi}\}. \tag{17}$$

(6) Number of peaks (greater than the average) in $\boldsymbol{P_\xi}$:

$$F6 := \sum_{i=1}^{\zeta-1} \delta\left(3 - D_1(i) + D_2(i) + D_3(i)\right), D_1(i) = \begin{cases} 1, & P_\xi(i) > \tilde{\boldsymbol{P}}_{\boldsymbol{\xi}} \\ 0, & \text{otherwise} \end{cases}, \tag{18}$$

$$D_2(i) = \begin{cases} 1, & P_\xi(i+1) < P_\xi(i) \\ 0, & \text{otherwise} \end{cases}, D_3(i) = \begin{cases} 1, & P_\xi(i-1) < P_\xi(i) \\ 0, & \text{otherwise,} \end{cases}. \tag{19}$$

(7) Frequency of the component with the highest energy in $\boldsymbol{P_t}$:

$$F7 := \frac{I_3 F_s}{\zeta - 1}, I_3 = \arg\max\{P_t(i) : 0 \le i \le \zeta - 1\}, \tag{20}$$

where F_s denotes the sampling frequency.

(8) Centroid frequency of $\boldsymbol{P_t}$:

$$F8 := \frac{\sum_{i=0}^{\zeta-1} P_t(i)\,\xi(i)}{\sum_{i=0}^{\zeta-1} P_t(i)}, \xi(i) = \frac{iF_s}{\zeta - 1}. \tag{21}$$

(9) Frequency standard deviation of $\boldsymbol{P_t}$:

$$F9 := \sqrt{\frac{\sum_{i=0}^{\zeta-1} P_t(i)\left(\xi(i) - F8\right)^2}{\sum_{i=0}^{\zeta-1} P_t(i)}}. \tag{22}$$

(10) Information entropy of $\boldsymbol{P_t}$:

$$F10 := -\sum_{i=0}^{\zeta-1} Q\left(P_t(i)\right) \log Q\left(P_t(i)\right), Q\left(P_t(i)\right) = \frac{D_4(i)}{\zeta}, \tag{23}$$

where $D_4(i)$ represents the number of repetitions of $P_t(i)$ in $\boldsymbol{P_t}$.

2.3. Proposed AFD-GCN scheme

In this subsection, the AFD-GCN scheme is proposed. This comprehensive framework comprises three key parts: AFD-based feature extraction, GCN and PQD recognition, as shown in Fig. 2. AFD-based signal analysis

Preprint not peer reviewed

This preprint research paper has not been peer reviewed. Electronic copy available at: https://ssrn.com/abstract=5229636

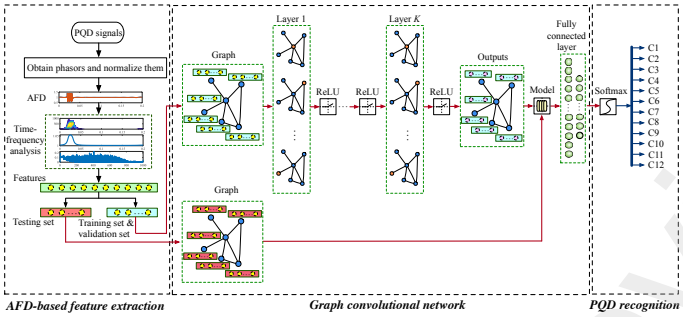


Figure 2: Framework of the AFD-GCN scheme.

and feature extraction have been detailed in the previous subsection, and we will introduce the GCN part (refer to [32] for details).

By applying convolution operations directly on the graph structure, GCN learns representations of both individual nodes and the entire graph. A graph consists of nodes and edges, represented as $G = (\boldsymbol{V}, \boldsymbol{E}, \boldsymbol{X})$, where $\boldsymbol{V} = \{v_j\}_{j=1}^{J}$ is the set of nodes, $\boldsymbol{E}$ is the set of edges, and $\boldsymbol{X} = \{\boldsymbol{x}_j\}_{j=1}^{J}$ is the set of feature matrices. It is worth noting that for the j-th node, $\boldsymbol{x}_j \in \mathbb{R}^{\boldsymbol{n}\times\boldsymbol{m}}$ is the feature matrix of v_j. The information of $\boldsymbol{V}$ and $\boldsymbol{E}$ forms a graph, which can be represented by an adjacency matrix $\boldsymbol{A} \in \mathbb{R}^{J\times J}$. Let A_{ij} be an element of $\boldsymbol{A}$ with $i, j \in [1, J]$ and $i \neq j$. Then, $A_{ij} = 1$, if and only if there is an edge between v_i and v_j; Otherwise, $A_{ij} = 0$.

A GCN layer takes $\{\boldsymbol{X}, \boldsymbol{A}\}$ as input and outputs the node embedding matrix $\boldsymbol{Z}$, which can be interpreted as an approximation of the nonlinear function $z(\boldsymbol{X}, \boldsymbol{A})$. For $k \in [1, K]$, the output of the k-th GCN layer is

$$\boldsymbol{Z}^{k+1} = z\left(\boldsymbol{Z}^{k}, \boldsymbol{A}\right) := \sigma\left(\widetilde{\boldsymbol{A}}\boldsymbol{Z}^{k}\boldsymbol{W}^{k}\right). \tag{24}$$

Here, the symmetric normalized adjacency matrix $\widetilde{\boldsymbol{A}} = \widehat{\boldsymbol{D}}^{-\frac{1}{2}}\widehat{\boldsymbol{A}}\widehat{\boldsymbol{D}}^{-\frac{1}{2}}$, where the degree matrix $\widehat{\boldsymbol{D}} = diag\left(d_1, d_2, \ldots, d_J\right)$, $d_i = \sum_{j=1}^{J}\widehat{\boldsymbol{A}}_{ij}$, $\widehat{\boldsymbol{A}} = \boldsymbol{A} + \boldsymbol{I}$. $\boldsymbol{I}$ is the identity matrix. $\boldsymbol{Z}^k$ is the input of the k-th layer with $\boldsymbol{Z}^1 = \boldsymbol{X}$. $\boldsymbol{W}^k$ is the weight matrix of the k-th layer, and $\sigma(\cdot)$ denotes the nonlinear activation function, such as ReLU. After propagating the feature $\boldsymbol{X}$ through K layers, the output $\boldsymbol{Z}^K$ is obtained. This output can then be fed into a fully connected layer to obtain $\boldsymbol{Y} := \boldsymbol{Z}^K\boldsymbol{W} + \boldsymbol{b}$, where $\boldsymbol{Y}$ and $\boldsymbol{W}$ denote the output and weight matrix of the fully connected layer, respectively. $\boldsymbol{b}$ is the bias vector. In the last part of Fig. 2, $\boldsymbol{Y}$ is used as the input of the softmax function to

Preprint not peer reviewed

This preprint research paper has not been peer reviewed. Electronic copy available at: https://ssrn.com/abstract=5229636

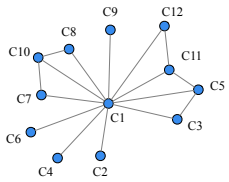


Figure 3: Graph construction of relationships between different PQDs.

obtain the score of each disturbance, where the maximum probability score determines the correct classification of the disturbances.

From (24), the classification accuracy of GCN depends on both effective features and an accurate graph structure. From Table 1, we observe that all PQDs are generated by modifying the waveform of the normal signal, indicating that C2 - C12 are all related to C1. Specifically, C3 and C5 share the same expression, with their difference lying in the range of α, suggesting a relationship between them. Similarly, C11 and C12 represent periodic superpositions of positive and negative disturbances on C1, respectively, indicating a correlation between them. In addition, both C5 and C11 exhibit significant amplitude drops, indicating a connection between these two. The essence of C7 is the superposition of interharmonic components in C1, while C10 is the superposition of harmonic components in C1, revealing a link between the two. Similarly, C8 is the superposition of harmonic components in C1 within a specific time period, which shows a correlation between C8 and C10. Based on the above observations, we construct a graph to describe the relationship between different PQDs, as shown in Fig. 3.

3. Experiments

In the task of training models, the source of data directly influences the model's effectiveness. Collecting a large amount of real-world data for each type of PQD is evidently challenging. To evaluate the performance of the AFD-GCN scheme in recognizing PQDs, we randomly generated 1000 samples for each type of PQD in MATLAB based on the mathematical model provided in Table 1. Among these samples, 600 were used for training, 200 for validation, and 200 for testing. In addition to noise-free samples, PQD signals with superimposed signal-to-noise ratios (SNRs) of 10 dB, 20 dB, and 30 dB were generated under the same conditions. This data generation method is well-established and widely adopted in PQD recognition research

Preprint not peer reviewed

This preprint research paper has not been peer reviewed. Electronic copy available at: https://ssrn.com/abstract=5229636

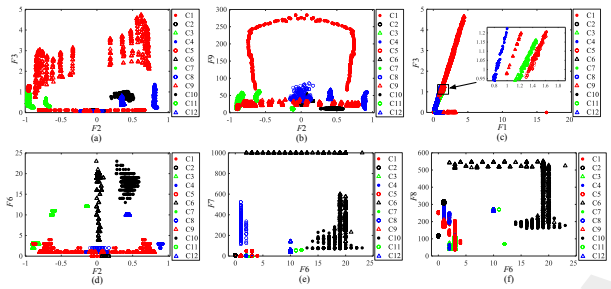


Figure 4: Visualization of different PQDs in two different feature dimensions. (a) ($F2$, $F3$). (b) ($F2$, $F9$). (c) ($F1$, $F3$). (d) ($F2$, $F6$). (e) ($F6$, $F7$). (f) ($F6$, $F8$).

[8, 19, 20]. The experiments were conducted in MATLAB 2021a, and the AFD-GCN model was trained using three GCN layers for 500 iterations.

3.1. AFD-based feature analysis

The AFD-based feature extraction method is applied to the generated noise-free signal to obtain features. Seven features are selected from the extracted features for visualization, namely $F1$, $F2$, $F3$, $F6$, $F7$, $F8$, and $F9$, as shown in Fig. 4. Fig. 4 (a) shows 12 different PQDs from the perspectives of $F2$ and $F3$, where C4, C9, and C11 can easily be distinguished. In addition, C3 and C5 are also distinct from other PQDs, but overlap with each other. Similarly, Fig. 4 (b) displays the perspective between $F2$ and $F9$, where C1, C7, C10 and C12 can be clearly differentiated. According to Fig. 4 (d), (e), and (f), the remaining C6, C8, and C2 can be distinguished from the perspectives of ($F2$, $F6$), ($F6$, $F7$), and ($F6$, $F8$), respectively. This indicates that only 7 features, namely $F1$,$F2$,$F3$,$F6$,$F7$,$F8$, and $F9$, are required to identify the 12 types of PQDs.

3.2. Graph construction analysis

To verify the effectiveness of the proposed graph (labeled as G1) shown in Fig. 3 for GCN to recognize different PQDs, three other graph constructions are proposed, labeled as G2, G3 and G4, as shown in Fig. 5 (a), (b) and (c), respectively. AFD-based features are selected as feature vectors for the four graphs, and are input into GCN for experiments. The results are shown in Fig. 6. The recognition accuracies of AFD-GCN under four different graphs are 100%, 99.17%, 99.67%, and 99.92%, respectively. Overall, with the establishment of connections between PQDs, the accuracy of recognition is increasing, which confirms the effectiveness of G1.

Preprint not peer reviewed

This preprint research paper has not been peer reviewed. Electronic copy available at: https://ssrn.com/abstract=5229636

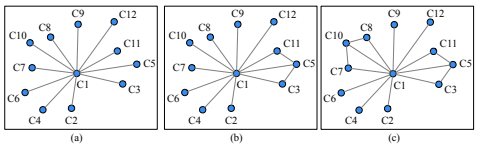


Figure 5: Graph construction of relationships between different PQDs. (a) Considering that all PQDs are only connected to C1. (b) Considering the connection relationship between C5 and C3, C11. (c) Considering the relationship between C10 and C7, C8.

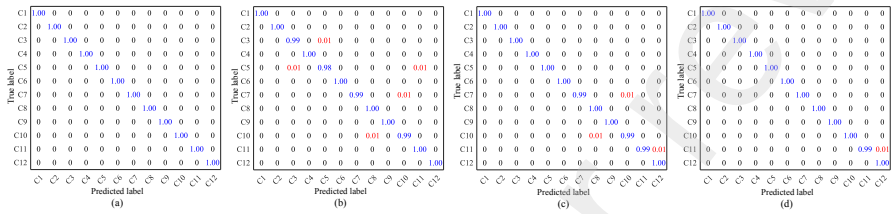


Figure 6: Recognition results under different graphs. (a) - (d) correspond to G1 - G4.

The proposal of AFD-GCN does not mean that the features used in the graph must be AFD-based. To evaluate the recognition capability of GCN with different features and graph structures, the features based on different methods, such as ST [20], HHT [21], WT [16], STFT [11] and AFD, are selected as the feature vectors for the graphs. The results are shown in Table 2. From Table 2, four key conclusions can be drawn. First, features based on ST, WT, HHT and STFT are compatible with GCN. Second, the accuracy of GCN is significantly influenced by the graph structure. Specifically, regardless of the feature type, the recognition accuracy of G1 consistently surpasses that of G2, G3, and G4. Third, GCN demonstrates strong noise resistance. Even under lower SNRs, its remains a excellent recognition performance. Fourth, AFD-based features exhibit excellent classification performance. For the same PQD dataset, AFD-based features consistently outperform the other four feature types across different graph structures. These findings not only verify the effectiveness of G1, but also confirm the feasibility of the AFD-GCN scheme.

3.3. Performance analysis

In addition to the input features and graph, the performance of GCN is also influenced by the number of hidden layers K and the weight matrix $\boldsymbol{W}^k$ of the k-th layer, $\boldsymbol{W}^k = \sqrt{\frac{\lambda_k}{N_{(k,\text{in})}N_{(k,\text{out})}}}\boldsymbol{U}_k$, where λ_k denotes the weighted

Preprint not peer reviewed

This preprint research paper has not been peer reviewed. Electronic copy available at: https://ssrn.com/abstract=5229636

Table 2: Comparison of different feature extraction methods under different graphs.

Features		Accuracy (%)				Features		Accuracy (%)			
		G1	G2	G3	G4			**G1**	G2	G3	G4
10 dB	ST	90.43	74.09	78.55	85.31	30 dB	ST	96.12	94.47	94.83	95.71
	WT	93.56	76.32	85.15	88.04		WT	99.83	93.81	96.53	97.66
	HHT	68.89	50.91	57.67	67.41		HHT	79.46	65.76	74.67	76.40
	STFT	96.16	79.79	85.07	88.94		STFT	99.34	96.62	97.94	98.17
	AFD	**96.70**	80.12	84.57	91.34		**AFD**	**100**	98.76	99.42	99.61
20 dB	ST	95.05	92.57	92.41	94.47	Clean	ST	99.59	98.17	99.26	99.38
	WT	99.34	92.24	96.20	98.60		WT	99.93	95.21	98.93	99.42
	HHT	77.31	57.10	68.23	76.32		HHT	98.91	88.61	96.37	97.19
	STFT	98.27	95.05	95.75	96.04		STFT	99.95	98.51	98.60	99.17
	AFD	**99.59**	97.19	98.02	98.84		**AFD**	**100**	99.17	99.67	99.92

Table 3: Comparison of accuracy under different GCN parameters.

K	Accuracy (%) under different λ									
	1	2	3	4	5	**6**	7	8	9	10
2	95.71	95.71	95.63	95.63	95.43	95.71	95.71	95.71	95.71	95.71
3	99.42	99.50	99.43	99.59	99.67	**99.59**	99.50	99.59	99.50	99.42
4	98.27	98.68	98.93	91.01	98.43	98.35	97.28	98.98	98.60	91.71
5	81.27	80.00	70.87	92.66	93.73	91.75	72.67	84.24	90.43	71.45

parameter of k-th layer. $N_{(k,\text{in})}$ and $N_{(k,\text{out})}$ represent the number of input and output features of the k-th layer, respectively. $\boldsymbol{U}_k$ is a random number matrix. Thus, for a given $\boldsymbol{U}_k$, the weight is determined by λ_k. Assume that the weighted parameter λ_k of each GCN layer is the same, denoted as λ. To analyze the impact of K and $\boldsymbol{W}^k$ on the model accuracy, AFD-based features at SNR = 20 dB and G1 are selected as inputs, and the simulations are conducted with different K and λ. The results are shown in Table 3.

From Table 3, it can be seen that larger values of λ and K do not necessarily result in higher accuracy in the GCN model. The key to enhancing the accuracy lies in appropriate parameter selection. For this study, the selected parameters are $\lambda = 6$ and $K = 3$. To analyze the performance of model training at different hidden layer levels K, the model is trained with

Preprint not peer reviewed

This preprint research paper has not been peer reviewed. Electronic copy available at: https://ssrn.com/abstract=5229636

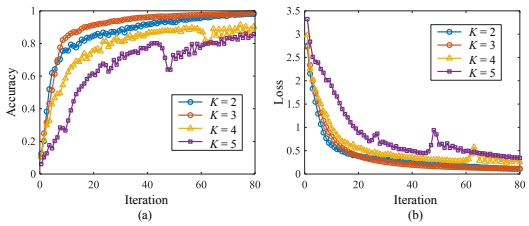


Figure 7: Accuracy and loss curves during training. (a) Accuracy curve. (b) Loss curve.

$\lambda = 6$. The verification accuracy and loss curves during the training process are shown in Fig. 7. Fig. 7 (a) shows that the accuracy is most stable when $K = 3$. Once the number of iterations reaches 80, the accuracy surpasses 99%, which indicates that selecting an appropriate number of GCN layers can significantly enhance the training speed. Fig. 7 (b) reveals that when $K = 2$ and 3, the models exhibit the lowest loss, implying that the models have effectively learned more information from the features. Overall, the AFD-GCN scheme with three hidden layers is proven to be the most effective scheme for PQD recognition.

In order to comprehensively evaluate the proposed scheme and compare it with popular schemes, experiments are conducted using synthetic PQD signals generated through Monte Carlo simulations. The results are shown in Table 4, where N_c denotes the number of the features. From Table 4, we can observe that when SNR = 20 dB, the accuracy of various PQD recognition schemes, including AFD-GCN, FFT-DT, FFT-ANN, DWT-RF, and ST-ANN, exceeds 90%. Among them, the accuracy of the proposed scheme is the highest, exceeding 99%. However, other schemes exhibit greater sensitivity to noise, particularly HT-RBF, EMD-PNN, and VMD-DT. Compared to other machine learning schemes, AFD-GCN not only demonstrates higher accuracy but also offers the advantages of shorter training and testing times.

3.4. Real-world signal classification

To verify the feasibility of the proposed AFD-GCN scheme in real-world scenarios, a hardware testing platform was constructed, as shown in Fig. 8. The platform consists of three parts, namely PQD signal source, data acquisition and processing device, and PC. The PQD signal source DG 811 is employed to generate 12 distinct PQD signals, with 100 samples collected for each disturbance. After acquiring the PQD signals, the waveform is displayed using the TDS 1002B and subsequently sampled and processed by

Preprint not peer reviewed

This preprint research paper has not been peer reviewed. Electronic copy available at: https://ssrn.com/abstract=5229636

Table 4: Comparison with other schemes under synthetic signals.

Scheme	N_c	SNR (dB)	Training time (s)	Testing time (s)	Accuracy
WT-SVM [17]	2	20	42.1959±1.5315	0.0328±0.0043	0.8918±0.0183
DWT-RF [15]	9	20	2.2861±0.1342	0.1810±0.0236	0.9146±0.0050
DWT-PNN [16]	9	30	2.2025±0.0116	0.3931±0.0243	0.8925±0.0029
ST-DT [19]	5	30	0.2846±0.0061	0.0061±0.0007	0.9042±0.0118
ST-ANN [18]	3	20	24.1917±0.7447	0.0284±0.0082	0.9098±0.0156
ST-PNN [20]	4	30	1.1810±0.0045	0.3690±0.0152	0.8885±0.0045
FFT-DT [9]	16	20	0.4023±0.0027	0.0011±0.0002	0.9658±0.0015
FFT-ANN [9]	16	20	38.4801±1.0634	0.0334±0.0065	0.9785±0.0057
HT-RBF [23]	4	Clean	58.8511±0.8955	0.1846±0.0052	0.9801±0.0051
EMD-PNN [21]	9	Clean	1.5503±0.0026	0.3124±0.0083	0.9581±0.0088
VMD-DT [22]	12	Clean	0.3548±0.0015	0.0014±0.0065	0.9930±0.0020
AFD-GCN	10	20	3.6607±0.1831	0.0026±0.0015	0.9972±0.0013

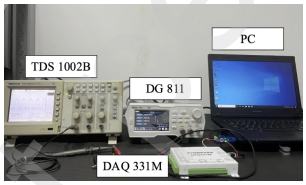


Figure 8: Hardware platform for experiment.

the DQA 331M. Finally, the collected signals are transmitted to the PC for PQD recognition using AFD-GCN, with 60 samples allocated for training, 20 for validation, and 20 for testing. For comparative analysis, under the same conditions, PQD recognition is performed using FFT-DT, FFT-ANN, DWT-RF, and ST-ANN. The results are shown in Table 5.

As can be seen from Table 5, the AFD-GCN scheme outperforms the other comparison schemes in terms of both recognition accuracy for each type of PQD and overall accuracy. However, the results in Table 5 are slightly lower than those given in Table 4. This difference can be attributed to two factors: the limited number of PQD test samples in real world scenarios and the inherent differences between real and synthetic signals. Nevertheless, the AFD-GCN scheme achieves satisfactory recognition results for real-world PQD signals, which confirms its feasibility for practical applications.

Preprint not peer reviewed

This preprint research paper has not been peer reviewed. Electronic copy available at: https://ssrn.com/abstract=5229636

Table 5: Comparison with other schemes under real-world signals.

Scheme	Accuracies (%) of the different PQDs												
	C1	C2	C3	C4	C5	C6	C7	C8	C9	C10	C11	C12	Total
FFT-DT	85	95	95	100	90	95	80	100	100	95	95	100	94.17
FFT-ANN	100	95	100	100	95	95	75	100	100	95	90	100	95.42
DWT-RF	90	90	100	95	70	95	75	90	100	95	90	100	90.83
ST-ANN	85	95	100	100	80	60	65	75	100	95	90	100	87.08
AFD-GCN	**100**	**100**	**100**	**100**	**100**	**95**	**100**	**100**	**100**	**95**	**100**	**100**	**99.17**

4. Conclusion

This article proposes a novel scheme for PQD recognition based on AFD and GCN. First, TTFD and MDs are introduced for signal analysis based on Core AFD. Subsequently, the phasor of PQD signals is analyzed through TTFD and MDs, and 10 features for PQD recognition are proposed. Second, GCN is employed to identify different PQDs. Third, by analyzing the signal model, a graph is proposed to represent the structural relationships between different PQDs. Finally, this graph, combined with AFD-based features, serves as the input to GCN for PQD recognition. Experimental results show that the proposed AFD-GCN scheme can accurately identify different PQDs in both synthetic and real-world signals, while maintaining excellent robustness in the presence of significant noise. Compared to several other popular schemes, the AFD-GCN scheme not only achieves superior recognition performance, but also exhibits lower computational costs. The experimental results confirm the effectiveness and practicality of the proposed scheme.

CRediT authorship contribution statement

Yanjiang Qiu: Conceptualization, Data curation, Formal analysis, Methodology, Software, Validation and Writing - Original Draft. Chitin Hon: Investigation, Resources, Validation and Funding acquisition. Tao Qian: Methodology, Validation, Investigation, Writing - review and editing, Visualization, Funding acquisition and Supervision.

Preprint not peer reviewed

This preprint research paper has not been peer reviewed. Electronic copy available at: https://ssrn.com/abstract=5229636

Declaration of competing interest

The authors declare that they have no known competing financial interests or personal relationships that could have appeared to influence the work reported in this paper.

Acknowledgments

The research is supported by the Science and Technology Development Fund of Macau SAR [grant number FDCT0128/2022/A, 0020/2023/RIB1, 0111/2023/AFJ, 005/2022/ALC], Major Project of Guangzhou National Laboratory [grant number GZNL2024A01004].

References

[1] N. Mlilo, J. Brown, T. Ahfock, Impact of intermittent renewable energy generation penetration on the power system networks–a review, Technology and Economics of Smart Grids and Sustainable Energy 6 (1) (2021) 25.

[2] T. Ravi, K. S. Kumar, C. Dhanamjayulu, B. Khan, K. Rajalakshmi, Analysis and mitigation of pq disturbances in grid connected system using fuzzy logic based iupqc, Scientific Reports 13 (1) (2023) 22425.

[3] X. Liang, C. Andalib-Bin-Karim, Harmonics and mitigation techniques through advanced control in grid-connected renewable energy sources: A review, IEEE Transactions on Industry Applications 54 (4) (2018) 3100–3111.

[4] K. Guerra, P. Haro, R. Gutiérrez, A. Gómez-Barea, Facing the high share of variable renewable energy in the power system: Flexibility and stability requirements, Applied Energy 310 (2022) 118561.

[5] A. Allahham, The german northwestern grid modelling & transient stability: Virtual synchronous machines (vsms) penetration, Ph.D. thesis, Carl-von-Ossietzky Universität Oldenburg (2023).

[6] S. Wang, H. Chen, A novel deep learning method for the classification of power quality disturbances using deep convolutional neural network, Applied energy 235 (2019) 1126–1140.

Preprint not peer reviewed

This preprint research paper has not been peer reviewed. Electronic copy available at: https://ssrn.com/abstract=5229636

[7] S. Li, X. Zhu, D. Zhou, Power quality disturbance signal denoising and detection based on improved dbo-vmd combined with wavelet thresholding, Electric Power Systems Research 238 (2025) 111193.

[8] Y. Liu, T. Jin, M. A. Mohamed, Q. Wang, A novel three-step classification approach based on time-dependent spectral features for complex power quality disturbances, IEEE Transactions on Instrumentation and Measurement 70 (2021) 1–14. doi:10.1109/TIM.2021.3050187.

[9] F. A. S. Borges, R. A. S. Fernandes, I. N. Silva, C. B. S. Silva, Feature extraction and power quality disturbances classification using smart meters signals, IEEE Transactions on Industrial Informatics 12 (2) (2016) 824–833. doi:10.1109/TII.2015.2486379.

[10] D. Granados-Lieberman, R. Romero-Troncoso, R. Osornio-Rios, A. Garcia-Perez, E. Cabal-Yepez, Techniques and methodologies for power quality analysis and disturbances classification in power systems: a review, IET Generation, Transmission & Distribution 5 (4) (2011) 519–529.

[11] D. D. Jayasree, Classification of power quality disturbance signals using fft, stft, wavelet transforms and neural networks - a comparative analysis, in: International Conference on Computational Intelligence and Multimedia Applications (ICCIMA 2007), Vol. 1, 2007, pp. 335–340. doi:10.1109/ICCIMA.2007.279.

[12] F. Jurado, J. R. Saenz, Comparison between discrete stft and wavelets for the analysis of power quality events, Electric power systems research 62 (3) (2002) 183–190.

[13] P. S. Wright, Short-time fourier transforms and wigner-ville distributions applied to the calibration of power frequency harmonic analyzers, IEEE transactions on instrumentation and measurement 48 (2) (1999) 475–478.

[14] O. Poisson, P. Rioual, M. Meunier, Detection and measurement of power quality disturbances using wavelet transform, IEEE Transactions on Power Delivery 15 (3) (2000) 1039–1044. doi:10.1109/61.871372.

Preprint not peer reviewed

This preprint research paper has not been peer reviewed. Electronic copy available at: https://ssrn.com/abstract=5229636

[15] M. Markovska, D. Taskovski, Z. Kokolanski, V. Dimchev, B. Velkovski, Real-time implementation of optimized power quality events classifier, IEEE Transactions on Industry Applications 56 (4) (2020) 3431–3442.

[16] S. Khokhar, A. A. M. Zin, A. P. Memon, A. S. Mokhtar, A new optimal feature selection algorithm for classification of power quality disturbances using discrete wavelet transform and probabilistic neural network, Measurement 95 (2017) 246–259.

[17] M. D. Borrás, J. C. Bravo, J. C. Montano, Disturbance ratio for optimal multi-event classification in power distribution networks, IEEE Transactions on Industrial Electronics 63 (5) (2016) 3117–3124.

[18] I. W. Lee, P. K. Dash, S-transform-based intelligent system for classification of power quality disturbance signals, IEEE Transactions on Industrial Electronics 50 (4) (2003) 800–805.

[19] F. Zhao, R. Yang, Power quality disturbance recognition using s-transform, in: 2006 IEEE Power Engineering Society General Meeting, IEEE, 2006, pp. 7–pp.

[20] S. Mishra, C. Bhende, B. Panigrahi, Detection and classification of power quality disturbances using s-transform and probabilistic neural network, IEEE Transactions on power delivery 23 (1) (2007) 280–287.

[21] M. Manjula, S. Mishra, A. Sarma, Empirical mode decomposition with hilbert transform for classification of voltage sag causes using probabilistic neural network, International Journal of Electrical Power & Energy Systems 44 (1) (2013) 597–603.

[22] P. D. Achlerkar, S. R. Samantaray, M. Sabarimalai Manikandan, Variational mode decomposition and decision tree based detection and classification of power quality disturbances in grid-connected distributed generation system, IEEE Transactions on Smart Grid 9 (4) (2018) 3122–3132. doi:10.1109/TSG.2016.2626469.

[23] T. Jayasree, D. Devaraj, R. Sukanesh, Power quality disturbance classification using hilbert transform and rbf networks, Neurocomputing 73 (7-9) (2010) 1451–1456.

Preprint not peer reviewed

This preprint research paper has not been peer reviewed. Electronic copy available at: https://ssrn.com/abstract=5229636

[24] S. Suganthi, A. Vinayagam, V. Veerasamy, A. Deepa, M. Abouhawwash, M. Thirumeni, Detection and classification of multiple power quality disturbances in microgrid network using probabilistic based intelligent classifier, Sustainable Energy Technologies and Assessments 47 (2021) 101470.

[25] S. Karasu, Z. Saraç, Classification of power quality disturbances by 2d-riesz transform, multi-objective grey wolf optimizer and machine learning methods, Digital signal processing 101 (2020) 102711.

[26] H. Erişti, Ö. Yıldırım, B. Erişti, Y. Demir, Optimal feature selection for classification of the power quality events using wavelet transform and least squares support vector machines, International Journal of Electrical Power & Energy Systems 49 (2013) 95–103.

[27] W. Qiu, Q. Tang, J. Liu, W. Yao, An automatic identification framework for complex power quality disturbances based on multifusion convolutional neural network, IEEE Transactions on Industrial Informatics 16 (5) (2019) 3233–3241.

[28] T. Qian, Adaptive fourier decompositions and rational approximations, part i: Theory, International Journal of Wavelets, Multiresolution and Information Processing 12 (05) (2014) 1461008.

[29] L. Zhang, W. Hong, W. Mai, T. Qian, Adaptive fourier decomposition and rational approximation—part ii: Software system design and development, International Journal of Wavelets, Multiresolution and Information Processing 12 (05) (2014) 1461009.

[30] P. Dang, T. Qian, Y. Y. Guo, Transient time-frequency distribution based on mono-component decompositions, International Journal of Wavelets, Multiresolution and Information Processing 11 (03) (2013) 1350022.

[31] I. P. Quality, Ieee recommended practice for monitoring electric power quality, IEEE recommended practice for monitoring electric power quality (1995).

[32] T. N. Kipf, M. Welling, Semi-supervised classification with graph convolutional networks, arXiv preprint arXiv:1609.02907 (2016).

Preprint not peer reviewed

This preprint research paper has not been peer reviewed. Electronic copy available at: https://ssrn.com/abstract=5229636